Direct comparison of two spin-squeezed optical clock ensembles at the 10^{-17} level

John M. Robinson [●] [✉]**, Maya Miklos** [●]**, Yee Ming Tso** [●]**, Colin J. Kennedy,**
Tobias Bothwell, Dhruv Kedar [●]**, James K. Thompson** [●] **& Jun Ye** [●] [✉]

Building scalable quantum systems that demonstrate performance enhancement based on entanglement is a major goal in quantum computing and metrology. The main challenge arises from the fragility of entanglement in large quantum systems. Optical atomic clocks utilizing a large number of atoms have pushed the frontier of measurement science, building on precise engineering of quantum states and control of atomic interactions. However, state-of-the-art optical atomic clocks are limited by a fundamental source of noise stemming from fluctuations of the population of many atoms—the quantum projection noise. Here, we present an optical clock platform integrated with collective strong-coupling cavity quantum electrodynamics for quantum non-demolition measurements. Optimizing the competition between spin measurement precision and loss of coherence, we measure a metrological enhancement for a large ensemble of atoms beyond the initial coherent spin state. Furthermore, a movable lattice allows the cavity to individually address two independent subensembles, enabling us to spin squeeze two clock ensembles successively and compare their performance without the influence of clock laser noise. Although the clock comparison remains above the effective standard quantum limit, the performance directly verifies 1.9(2) dB clock stability enhancement at the 10^{-17} level without subtracting any technical noise contributions.

Optical atomic clocks are rapidly advancing the frontier of measurement science with continued progress in their precision and accuracy. Accuracy evaluations at the 10^{-18} level[1–3] and frequency ratio measurements in networks of atomic clocks are setting the stage for the redefinition of the SI second based on optical technology[4,5]. In addition to time-keeping, advanced atomic clocks are also being employed for tests of fundamental symmetry and searches for new physics, as well as applications in relativistic geodesy and quantum information science[6–9]. Clock precision on the 21st digit has recently enabled the measurement of the gravitational redshift within a single atomic ensemble at the submillimetre length scale[10]. Improving the fundamental limits of optical clock stability promises to open new opportunities in physics.

A fundamental noise source in atomic clocks is the quantum projection noise (QPN) that stems from the inherent population fluctuations associated with the projective measurement of N uncorrelated atoms[11]. As QPN-limited stability scales as $1/\sqrt{N}$, operating with a higher atom number N is advantageous. However, technical noise from imperfect state readout, intrinsic atom–atom interactions, or aliased frequency noise of the interrogating clock laser pose challenges for observing clock performance at the QPN limit[12]. With precise engineering of quantum states and control of atomic interactions[13], and using laser-noise mitigation techniques such as synchronous comparisons[14,15], state-of-the-art optical clocks are currently approaching QPN-limited stability with up to 10^5 atoms[10].

The development of quantum entanglement has provided an exciting new direction for reducing the impact of QPN in quantum sensors, offering the opportunity to greatly advance this state-of-the-art performance[16,17]. A particular form of entanglement, the spin-squeezed
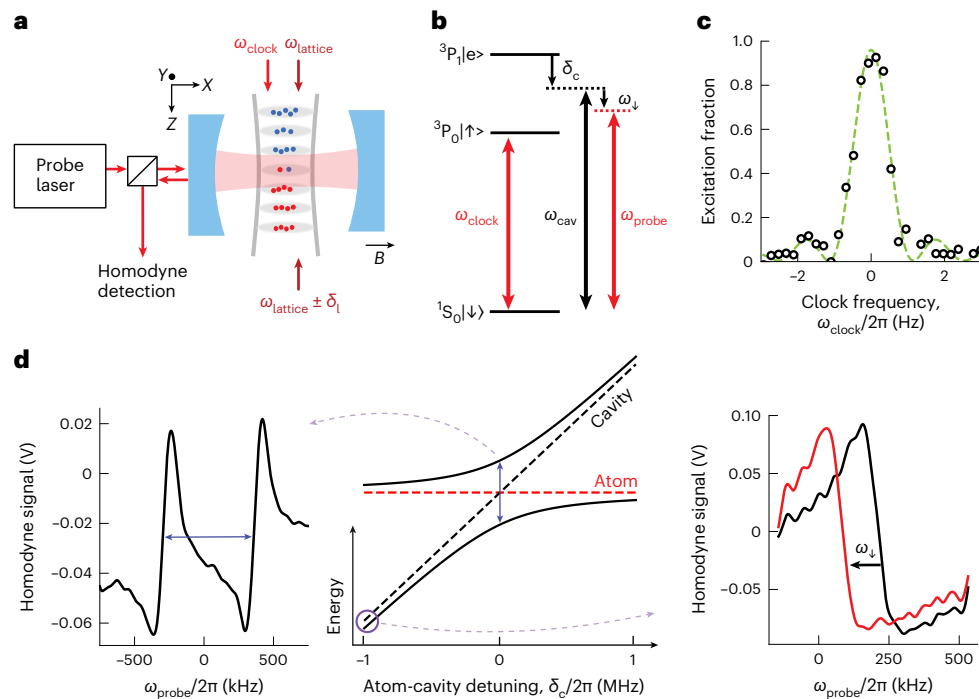
JILA, National Institute of Standards and Technology and University of Colorado, Department of Physics, University of Colorado, Boulder, CO, USA.
[✉]e-mail: john.robinson@colorado.edu; Ye@jila.colorado.edu

Fig. 1 | Optical clock with cQED architecture. a, ^{87}Sr atoms are trapped in a movable vertical optical lattice (by detuning one lattice beam by δ_l), enabling both independent squeezing and readout of two subensembles (red and blue) within the atomic cloud. The clock laser propagates along the vertical lattice, providing a global drive of the clock transition. Populations are measured non-destructively by means of homodyne detection of the laser probing the atom–cavity system. **b,** The relevant energy levels of ^{87}Sr. We prepare coherent superpositions between the clock states $|\downarrow\rangle$ and $|\uparrow\rangle$. The frequency of the optical cavity ω_{cav} is tuned near the $|\downarrow\rangle \rightarrow |e\rangle$ transition to realize the atom–cavity coupled system. Atoms in the ground state $N_\downarrow$ shift the cavity frequency by an amount $\omega_\downarrow$, whereas atoms in $|\uparrow\rangle$, the other optical clock state, do not couple to the cavity. **c,** Rabi spectroscopy of the clock transition with a Fourier-limited linewidth of 1 Hz using a π-pulse of 0.8 s. Open black circles indicate the measured data, with the corresponding Rabi fit as the dashed green line. **d,** Left, the measured vacuum Rabi splitting indicates that we are in the collective strong-coupling regime. Middle, avoided crossing behaviour of the atom–cavity system. Right, when the cavity was slightly detuned by $\delta_c = -2\pi \times 1$ MHz, we observed the dispersive shift of the cavity-like mode.

state (SSS), was proposed early on to utilize quantum correlation to conceal noise from individual atoms and thus achieve improved measurement precision and bandwidth[18,19]. The creation of entanglement for metrology has been explored in a wide variety of atomic quantum sensors including microwave clocks[20–27], ion clocks[28,29], magnetometers[30] and matter-wave interferometers[31,32].

Spin squeezing in atomic clocks has yet to yield enhancement at state-of-the-art stability levels. A spin-squeezed microwave clock has observed 11 dB of enhancement[26] at the 10^{-10} stability level at 1 s, in contrast to microwave fountain clocks at 10^{-14} (ref. 33). For optical clocks, which operate at much higher stability, generation of entanglement has been demonstrated by a measured metrological enhancement of −4.6 dB (ref. 34). After subtraction of a laser-noise model, an optical clock employing a SSS was inferred to operate −4.4 dB below the standard quantum limit (SQL) at a fractional frequency stability of $1.3 \times 10^{-13}\tau^{-1/2}$; this was achieved by interrogating 350 atoms with 0.17 ms dark time (where τ is the averaging time in seconds)[34]. To employ spin squeezing for practical metrological applications, we require substantially longer interrogation time and higher atom number. Also, as we improve the spin-squeezed clock performance, it becomes more difficult to manage contributions from technical noise. For example, a redshift measurement in a differential clock comparison requires rejection of Dick noise, which cannot be removed in post-processing[10,35].

In this work, we report the design and operation of a multiplexed spin-squeezed clock to advance toward these outstanding goals, employing 10^4 atoms interrogated for 14 ms. A collective, strongly-coupled cavity quantum electrodynamics (QED) system was used to perform quantum non demolition (QND) measurement of the clock state[36], providing spin squeezing and clock readout. We generated an SSS with a single ensemble of $N = 2 \times 10^4$ atoms and

directly measured a metrological enhancement of −1.7(7) dB, where 7 represents 1 sigma uncertainty, proving the creation of entanglement in this sample. A movable optical lattice intersecting the cavity mode was used to transport atomic ensembles into and out of the cavity mode to address multiple independent clock ensembles. By alternately shuttling two spatially separated subensembles in and out of the cavity, we demonstrated a direct comparison between two spin-squeezed optical clock ensembles at 1.9(3) dB below QPN and 0.7(3) dB above the effective SQL. This comparison averages with $1.3 \times 10^{-15}\tau^{-1/2}$ and reaches the level of 10^{-17} measurement precision. With future improvements on entanglement-enhanced measurements, this system is ideally suited to explore the interplay of gravity and quantum entanglement[10,35,37].

Our clock operated with up to 2×10^4 ^{87}Sr atoms confined in a vertical one-dimensional (1D) magic wavelength optical lattice (Fig. 1a). The clock laser[38] propagated along the vertical trapping lattice, globally addressing all of the atoms on the ultra-narrow $|\downarrow\rangle \equiv |^1S_0, m_F = -9/2\rangle$ to $|\uparrow\rangle \equiv |^3P_0, m_F = -9/2\rangle$ clock transition (Fig. 1b). mF is the magnetic quantum number. F represents the atomic state. We demonstrated Rabi spectroscopy at a Fourier-limited full-width at half-maximum of 1 Hz with a peak π-pulse transfer efficiency of 97(1)% (Fig. 1c). Although our squeezed-clock experiments currently operate at shorter interrogation times, this demonstrates the capability of achieving state-of-the-art laser-atom coherence times.

The key new features of the system are the combination of the state-of-the-art clock spectroscopy with QND-based spin squeezing and the capability of moving clocks with entangled atoms for direct comparison. The coupled atom–cavity system is realized by tuning the bare optical cavity near the $|\downarrow\rangle \rightarrow |e\rangle \equiv |^3P_1, m_F = -11/2\rangle$ transition ($\Gamma = 2\pi \times 7.48(1)$ kHz (ref. 39). The effective vacuum Rabi frequency for atom–cavity coupling is $2g = 2 \times (2\pi \times 5.1(2))$ kHz (Fig. 2a
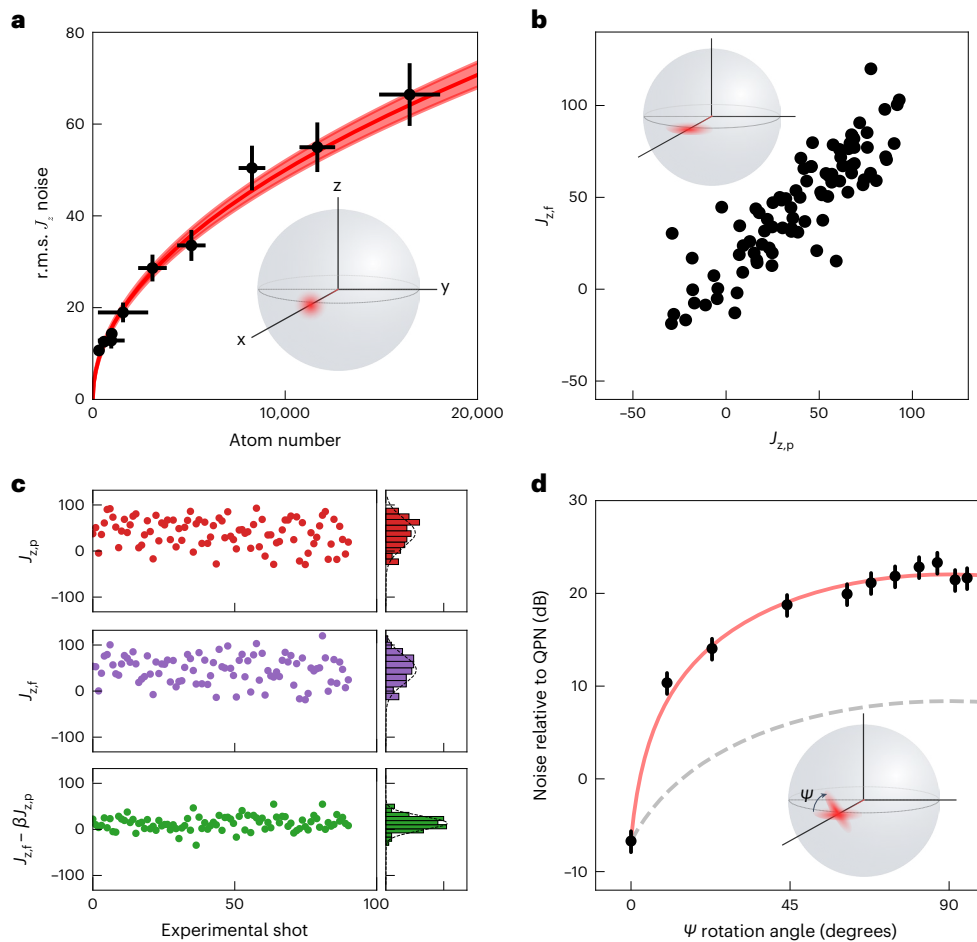
Fig. 2 | Non-demolition measurements of the collective spin state.
a, Measurement of the QPN fluctuations of the initial CSS. The red line shows expected dependence of $\Delta J_z = \sqrt{N}/2$, and the shaded area indicates the 1-sigma confidence interval due to uncertainty in the atom–cavity coupling. Inset, pictorial representation of the CSS on a Bloch sphere. **b**, The high-degree of correlations are shown between $J_{z,p}$ and $J_{z,f}$. Inset, SSS shown on the Bloch sphere.

c, The premeasurements $J_{z,p}$ (red), final measurements $J_{z,f}$ (purple) and the difference $J_{z,f} - \beta J_{z,p}$ (green) are shown for each experimental shot. **d**, State tomography of the SSS. The measured noise relative to the QPN as a function of rotation angle ψ. The solid red line is a fit to the measured data and the dashed grey line indicates a unitary spin-squeezed state. Error bars represent 1σ statistical confidence interval.

and Methods)[23,25,40,41]. With the bare cavity photon decay rate of $\kappa = 2\pi \times 158(7)$ kHz, we have a single-atom effective cooperativity of $\mathcal{C} = \frac{4g^2}{\kappa\Gamma} = 0.1$. For effective atom number $N = 10^4$, we are well into the collective strong-coupling regime with $N\mathcal{C} = 10^3$, as is clearly seen by the vacuum Rabi splitting (Fig. 1d).

To optimize the information that we gain about the collective spin state over the loss of coherence, we detuned the cavity resonance from $|\downarrow\rangle \rightarrow |e\rangle$ by $\delta_c = \omega_{cavity} - \omega_{atom} = -2\pi \times 1$ MHz (Fig. 1b). A fixed-frequency laser was then tuned on resonance of the cavity-like mode to measure the dispersive shift $\omega_\downarrow$ induced by the presence of atoms in the ground state. We express the number of atoms in $|\downarrow\rangle$ in terms of $\omega_\downarrow$ as $N_\downarrow = \omega_\downarrow \frac{\delta_c}{g^2}(1 + \frac{\omega_\downarrow}{\delta_c})$ (Methods). An optical π-pulse was then applied to swap the population between $|\uparrow\rangle$ and $|\downarrow\rangle$. The frequency shift was measured again to determine the excited state population $N_\uparrow$. We generated entanglement using conditional spin squeezing by making repeated QND measurements of the collective spin projection $J_z = (N_\downarrow - N_\uparrow)/2$ (ref. 24). Two repeated measurements of J_z contain highly correlated QPN, and hence their difference allows one to perform sub-QPN metrology[21,24].

To properly quantify spin squeezing, we first measured the QPN of a coherent spin state (CSS). A $\pi/2$ pulse prepared the CSS on the equator of the Bloch sphere and a measurement of J_z was performed. The measured fluctuations of the cavity frequency shift were converted to J_z using the atom–cavity coupling coefficient $g = 2\pi \times 5.1(2)$ kHz (Methods). We plot the root mean square (r.m.s.) noise of J_z versus the atom number in Fig. 2a, with the expected dependence $\Delta J_z = \sqrt{N}/2$ shown as the red line. The shaded region indicates the uncertainty in the atom number arising from the uncertainty in the atom–cavity coupling.

We now demonstrate repeated measurements of J_z with differential resolution well below QPN. After an initial $\pi/2$, we made a premeasurement denoted by $J_{z,p}$, waited a dwell time of 20 ms and performed the final measurement $J_{z,f}$ (Fig. 2b). The deviation of the mean J_z in Fig. 2b is due to a percent level error in the calibrated clock pulse duration. For the photon number of 2.3×10^4, the data was taken with a dwell time of 4 ms. We chose a relatively short dwell time and corresponding Ramsey dark time to minimize the effect of degraded correlations between the J_z measurements at dwell times greater than approximately 100 ms. Although the premeasurement fluctuates with standard deviation $\Delta J_{z,QPN} = \sqrt{N}/2$, the final measurement contains highly correlated QPN, as seen by the reduced noise in the difference between the two measurements (Fig. 2c). Spin-noise reduction is defined as $R = \left(\frac{\Delta(J_{z,f} - \beta J_{z,p})}{\Delta J_{z,QPN}}\right)^2$, where we used an optimal estimator β to account for differential technical noise. We
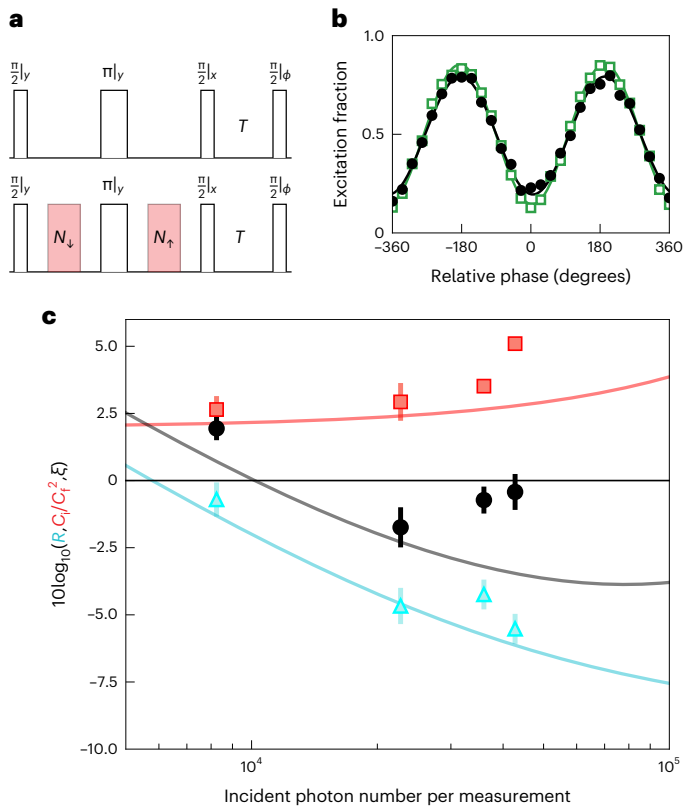
Fig. 3 | Directly observed metrological enhancement versus QND probe strength. a, The degree of atomic coherence was measured by scanning the Ramsey fringe with two distinct pulse sequences. Top, sequence with all optical rotations required for squeezing but with no probing applied. Bottom, sequence with QND probing. **b**, Ramsey fringes for the two corresponding pulse sequences taken at a probe photon number of 2.3×10^4 and a Ramsey dark time of $T = 14$ ms. The reduction of contrast at this probe power is 11(1)%. **c**, Relative spin-noise reduction R (cyan triangles), fractional contrast loss C_i/C_f^2 (red squares) and the corresponding metrological enhancement parameter ξ (black circles). At the optimal photon number, we directly measured a metrological enhancement of −1.7(7) dB. Expected R given our estimated quantum efficiency of $Q = 0.28$ (cyan line), expected contrast loss by means of free-space scattering (red line) and the corresponding expected metrological enhancement (black line, see Methods). Error bars represent 1σ statistical confidence interval.
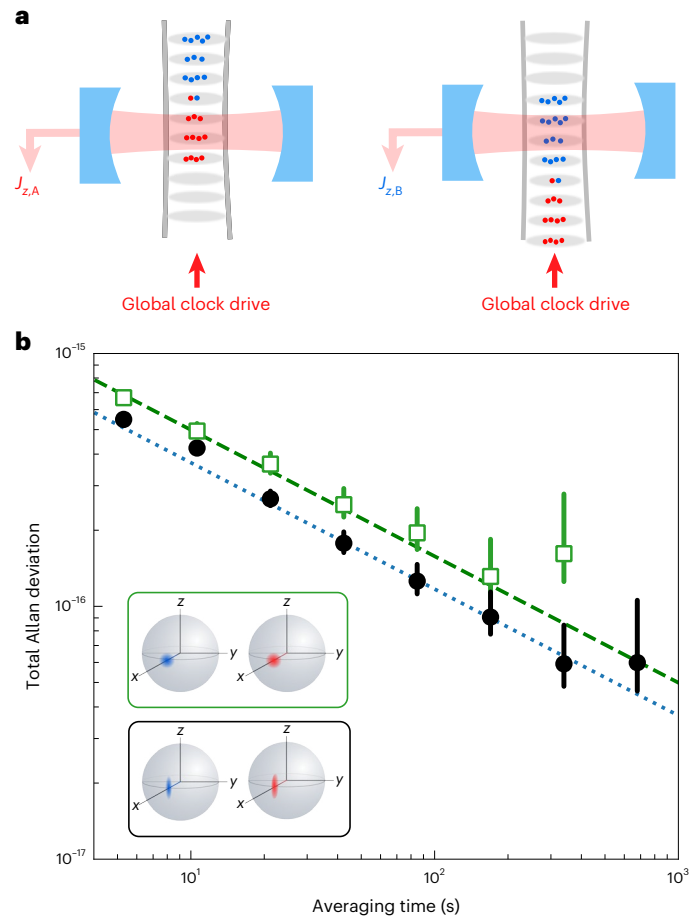
Fig. 4 | Differential clock comparison. a, The optical lattice was moved to shuttle the two subensembles in and out of the cavity, allowing independent squeezing and readout. The clock laser, coming from below, addressed both ensembles in a global fashion. **b**, Allan deviation of the CSS–CSS comparison (green open squares) and of the SSS–SSS comparison (black circles), showing an enhancement of 1.9(2) dB using spin squeezing. Theoretical QPN limit of the clock comparison (dashed green line) and the theoretical effective SQL limit (dotted blue line). The SSS–SSS measurement contained $n = 299$ data points (1,587 s) and the CSS–CSS measurement contained 159 data points (847 s), with the error bars corresponding to the standard deviation. The inset shows the different states on the Bloch sphere for each clock comparison. Error bars represent 1σ statistical confidence interval.

directly observed spin-noise reduction $R = -4.6(5)$ dB relative to QPN at the optimal squeezing photon number. Assuming that the detection noise between the two measurements is uncorrelated, we inferred the intrinsic spin-noise reduction of −6.6(5) dB. We performed state tomography to evaluate the amount of antisqueezing introduced by the QND measurement (Fig. 2d). The observed antisqueezing was well above the expected level given our estimated quantum efficiency of $Q = 0.28$, which indicates additional technical noise in the antisqueezing quadrature (Methods).

To verify that the measured spin-noise reduction arises from entanglement, one must weigh R against the loss of coherence induced by the probe, as measured by the Ramsey fringe contrast. The metrological enhancement is expressed as[21,23,25]

$$\xi = \left(\frac{\Delta(J_{z,f} - \beta J_{z,p})}{\Delta J_{z,QPN}} \right)^2 \frac{C_i}{C_f^2}, \tag{1}$$

where C_i and C_f are the initial and final contrast, respectively, measured by scanning the excitation fraction as a function of the phase of the final $\pi/2$ pulse. The metrological enhancement ξ serves as an entanglement

witness under the assumption that the QND probing does not enhance the spin correlations in the transverse plane[42]. In the definition of equation (1), $\xi = 1$ corresponds to an effective SQL for $C_i N$ atoms taking into account the non-unity C_i. Generating and using entanglement directly in the optical clock states requires performing several optical rotations that induce loss of Ramsey contrast due to single-particle motional effects in the 1D optical lattice, even without QND probing. This is in comparison with the generation of entanglement in a ground-state manifold, where the use of microwave rotations typically leads to less degradation of the atomic coherence[34,43]. To distinguish the effect of our QND probing on optical atomic coherence, we measured the Ramsey fringe contrast with and without probe, keeping all other rotations in the sequence (Fig. 3a). The initial contrast with no QND probing was $C_i = 0.71(1)$ (Fig. 3b). Turning on a QND probe with 2.3×10^4 photons per population measurement reduced the contrast to $C_f = 0.60(1)$. At this optimal probe power, the measured metrological enhancement reached −1.7(7) dB (Fig. 3c). This is a direct verification of spin entanglement in our system under the assumption that the QND probe leads to a monotonic decrease in the Ramsey contrast[42], which is shown in

Fig. 3c. The optimal estimator at this probe power was $\beta = 0.75$. Assuming uncorrelated detection noise in the two J_z measurements, we calculated the noise of the final measurement and subtracted it in quadrature, giving an inferred metrological enhancement of −3.7(7) dB.

To demonstrate the metrological gain from spin squeezing on clock performance, we performed a direct clock comparison between two spin-squeezed ensembles. Using the moving optical lattice, we addressed two independent subensembles labelled A and B (Fig. 4a) within the same atomic cloud, separated by a vertical distance of 150 μm (Methods). We performed differential clock comparisons between the two subensembles, contrasting the case where both are projected into SSSs (black circles) against the case of CSSs without the use of the QND probe (green open squares) (Fig. 4b). In either case, all rotations and transports that manipulate the states were performed identically, which allowed a direct measurement of the impact of spin squeezing on clock stability. The observed stability was $1.58(3) \times 10^{-15}\tau^{-1/2}$ and $1.27(2) \times 10^{-15}\tau^{-1/2}$ for the CSS–CSS and SSS–SSS comparisons, respectively. We directly observed an enhancement of stability by 1.9(2) dB in the SSS–SSS comparison over that of CSS–CSS. Note that this enhancement decibel value (and all others in this work) were calculated as $20\log_{10}(\sigma_{SSS-SSS}/\sigma_{CSS-CSS})$.

To put our results in the proper context, we sought to benchmark the observed SSS–SSS stability to both the practically achievable limit set by QPN and fundamental limit set by the effective SQL. The measurement of $(J_{z,A} - J_{z,B})$ was limited by the sum of independent squared QPN from each subensemble. The QPN-limited clock stability was calculated using equation (15) (Methods) and plotted as the dashed green line. With a measured $C_i = 0.55(1)$ for both ensembles, this set the bound of optimal practically achievable stability for CSS–CSS (dashed green line, Fig. 4b). However, the ultimate bound on the performance of an unentangled ensemble with $C_i < 1$ is the effective SQL. This stricter bound treats the $(1 - C_i)$ fraction of atoms as no longer participating in the pure CSS, which thus reduces the QPN due to the C_i fraction of atoms. The effective SQL-limited phase resolution was calculated using equation (14) from the Methods and plotted as the dotted blue line (Fig. 4b).

The observed stability of the CSS–CSS comparison was consistent with the QPN-limited stability and 2.6(3) dB above the effective SQL. Implementing QND-based squeezing operation and accounting for the final contrast of $C_f = 0.50(1)$, the SSS–SSS comparison shows a 1.9(3) dB gain over the QPN-limited stability, demonstrating notable enhancement of clock performance from the squeezing operation. This result is above the effective SQL by 0.7(3) dB.

The direct observation of the clock comparison below the QPN limit with measurement precision averaging down to the 10^{-17} level is a crucial step towards improving the performance of the best optical lattice clocks by means of entanglement. We built on the foundational work of implementing entanglement on optical clock operation[34], extending the interrogation time by a factor of ~100 and increasing the atom number by a factor of ~20, and altogether improved the stability by two orders of magnitude. By comparing two independent spin-squeezed ensembles, we could directly observe sub-QPN operation without subtracting a laser-noise model to infer the enhancement factor. This improved stability translates into increased sensitivity for many applications of interest. Squeezing in differential measurements between subensembles could aid in measuring the gravitational redshift at ever-shorter length scales[10,35] and any other spatially dependent systematic clock shifts. With sufficiently low link noise, the enhanced stability of our squeezed clock can improve synchronous clock comparisons within free space- or fibre-connected networks[5,28], gravitational wave detection[44] and secure time transfer through distributed entangled states[45].

We anticipate various improvements to the current apparatus that will enhance the level of squeezing and overall clock stability. Enhanced control of atomic motion will yield improved initial Ramsey contrast and increased coupling to the cavity mode. Further, larger atom number, improved single-atom cooperativity and higher quantum efficiency will all lead to stronger spin squeezing. The primary limitation to our dark time is degraded correlation between the pre and final measurement, which can be circumvented with technical improvements to the QND probe homodyne detection. Increasing the Ramsey dark time will push the spin-squeezed clock to the current best optical clock stability[10]. By integrating the exquisite stability of a competitive optical lattice clock with the all-to-all interactions enabled by cavity QED, this system opens the door for explorations of other flavours of entanglement-enhanced metrology[46–49] and offers tunability and flexibility for studies of a wide variety of many-body spin dynamics[50–55].

Online content

Any methods, additional references, Nature Portfolio reporting summaries, source data, extended data, supplementary information, acknowledgements, peer review information; details of author contributions and competing interests; and statements of data and code availability are available at https://doi.org/10.1038/s41567-023-02310-1.

References

1. Bothwell, T. et al. JILA SrI optical lattice clock with uncertainty of 2.0×10⁻¹⁸. *Metrologia* **56**, 065004 (2019).
2. Brewer, S. M. et al. ²⁷Al⁺ quantum-logic clock with a systematic uncertainty below 10⁻¹⁸. *Phys. Rev. Lett.* **123**, 033201 (2019).
3. McGrew, W. F. et al. Atomic clock performance enabling geodesy below the centimetre level. *Nature* **564**, 87–90 (2018).
4. Beloy, K. et al. Frequency ratio measurements at 18-digit accuracy using an optical clock network. *Nature* **591**, 564–569 (2021).
5. Roberts, B. M. et al. Search for transient variations of the fine structure constant and dark matter using fiber-linked optical atomic clocks. *New J. Phys.* **22**, 093010 (2020).
6. Sanner, C. et al. Optical clock comparison for Lorentz symmetry testing. *Nature* **567**, 204–208 (2019).
7. Kennedy, C. J. et al. Precision metrology meets cosmology: improved constraints on ultralight dark matter from atom-cavity frequency comparisons. *Phys. Rev. Lett.* **125**, 201302 (2020).
8. Takamoto, M. et al. Test of general relativity by a pair of transportable optical lattice clocks. *Nat. Photonics* **14**, 411–415 (2020).
9. Schine, N., Young, A. W., Eckner, W. J., Martin, M. J. & Kaufman, A. M. Long-lived Bell states in an array of optical clock qubits. *Nat. Phys.* **18**, 1067–1073 (2022).
10. Bothwell, T. et al. Resolving the gravitational redshift across a millimetre-scale atomic sample. *Nature* **602**, 420–424 (2022).
11. Itano, W. M. et al. Quantum projection noise: population fluctuations in two-level systems. *Phys. Rev. A* **47**, 3554–3570 (1993).
12. Al-Masoudi, A., Dörscher, S., Häfner, S., Sterr, U. & Lisdat, C. Noise and instability of an optical lattice clock. *Phys. Rev. A* **92**, 063814 (2015).
13. Aeppli, A. et al. Hamiltonian engineering of spin-orbit-coupled fermions in a Wannier–Stark optical lattice clock. *Sci. Adv.* **8**, eadc9242 (2022).
14. Marti, G. E. et al. Imaging optical frequencies with 100 μHz precision and 1.1 μm resolution. *Phys. Rev. Lett.* **120**, 103201 (2018).
15. Oelker, E. et al. Demonstration of 4.8 ×10⁻¹⁷ stability at 1s for two independent optical clocks. *Nat. Photonics* **13**, 714–719 (2019).
16. Giovannetti, V. et al. Advances in quantum metrology. *Nat. Photonics* **5**, 222 (2011).
17. Polzik, E. S. et al. Entanglement and spin squeezing in a network of distant optical lattice clocks. *Phys. Rev. A* **93**, 021404 (2016).
18. Wineland, D. J., Bollinger, J. J., Itano, W. M., Moore, F. L. & Heinzen, D. J. Spin squeezing and reduced quantum noise in spectroscopy. *Phys. Rev. A* **46**, R6797–R6800 (1992).
19. Kitagawa, M. & Ueda, M. Squeezed spin states. *Phys. Rev. A* **47**, 5138–5143 (1993).

20. Appel, J. et al. Mesoscopic atomic entanglement for precision measurements beyond the standard quantum limit. *Proc. Natl Acad. Sci. USA* **106**, 10960–10965 (2009).

21. Leroux, I. D., Schleier-Smith, M. H. & Vuletić, V. Implementation of cavity squeezing of a collective atomic spin. *Phys. Rev. Lett.* **104**, 073602 (2010).

22. Leroux, I. D., Schleier-Smith, M. H. & Vuletić, V. Orientation-dependent entanglement lifetime in a squeezed atomic clock. *Phys. Rev. Lett.* **104**, 250801 (2010).

23. Schleier-Smith, M. H., Leroux, I. D. & Vuletić, V. States of an ensemble of two-level atoms with reduced quantum uncertainty. *Phys. Rev. Lett.* **104**, 073604 (2010).

24. Chen, Z., Bohnet, J. G., Sankar, S. R., Dai, J. & Thompson, J. K. Conditional spin squeezing of a large ensemble via the vacuum Rabi splitting. *Phys. Rev. Lett.* **106**, 133601 (2011).

25. Cox, K. C., Greve, G. P., Weiner, J. M. & Thompson, J. K. Deterministic squeezed states with collective measurements and feedback. *Phys. Rev. Lett.* **116**, 093602 (2016).

26. Hosten, O., Engelsen, N. J., Krishnakumar, R. & Kasevich, M. A. Measurement noise 100 times lower than the quantum-projection limit using entangled atoms. *Nature* **529**, 505–508 (2016).

27. Pezzè, L., Smerzi, A., Oberthaler, M. K., Schmied, R. & Treutlein, P. Quantum metrology with nonclassical states of atomic ensembles. *Rev. Mod. Phys.* **90**, 035005 (2018).

28. Nichol, B. C. et al. An elementary quantum network of entangled optical atomic clocks. *Nature* **609**, 689–694 (2022).

29. Marciniak, C. D. et al. Optimal metrology with programmable quantum sensors. *Nature* **603**, 604–609 (2022).

30. Wasilewski, W. et al. Quantum noise limited and entanglement-assisted magnetometry. *Phys. Rev. Lett.* **104**, 133601 (2010).

31. Greve, G. P., Luo, C., Wu, B. & Thompson, J. K. Entanglement-enhanced matter-wave interferometry in a high-finesse cavity. Preprint at arxiv.org/abs/2110.14027 (2021).

32. Malia, B. K., Wu, Y., Martínez-Rincón, J. & Kasevich, M. A. Distributed quantum sensing with mode-entangled spin-squeezed atomic states. *Nature* **612**, 661–665 (2022).

33. Weyers, S. et al. Advances in the accuracy, stability, and reliability of the PTB primary fountain clocks. *Metrologia* **55**, 789–805 (2018).

34. Pedrozo-Peñafiel, E. et al. Entanglement on an optical atomic-clock transition. *Nature* **588**, 414–418 (2020).

35. Zheng, X. et al. Differential clock comparisons with a multiplexed optical lattice clock. *Nature* **602**, 425–430 (2022).

36. Bowden, W., Vianello, A., Hill, I. R., Schioppo, M. & Hobson, R. Improving the *q* factor of an optical atomic clock using quantum nondemolition measurement. *Phys. Rev. X* **10**, 041052 (2020).

37. Colombo, S., Pedrozo-Peñafiel, E. & Vuletić, V. Entanglement-enhanced optical atomic clocks. *Appl. Phys. Lett.* **121**, 210502 (2022).

38. Matei, D. G. et al. 1.5 μm lasers with sub-10 mHz linewidth. *Phys. Rev. Lett.* **118**, 263202 (2017).

39. Norcia, M. A. & Thompson, J. K. Strong coupling on a forbidden transition in strontium and nondestructive atom counting. *Phys. Rev. A* **93**, 023804 (2016).

40. Hood, C. J., Chapman, M. S., Lynn, T. W. & Kimble, H. J. Real-time cavity QED with single atoms. *Phys. Rev. Lett.* **80**, 4157–4160 (1998).

41. Hu, J., Chen, W., Vendeiro, Z., Zhang, H. & Vuletić, V. Entangled collective-spin states of atomic ensembles under nonuniform atom-light interaction. *Phys. Rev. A* **92**, 063816 (2015).

42. Schleier-Smith, M. *Cavity-enabled Spin Squeezing for a Quantum-enhanced Atomic Clock*. PhD thesis, Massachusetts Institute of Technology (2011).

43. Braverman, B. et al. Near-unitary spin squeezing in ^{171}Yb. *Phys. Rev. Lett.* **122**, 223203 (2019).

44. Kolkowitz, S. et al. Gravitational wave detection with optical lattice atomic clocks. *Phys. Rev. D* **94**, 124043 (2016).

45. Kómár, P. et al. A quantum network of clocks. *Nat. Phys.* **10**, 582–587 (2014).

46. Davis, E., Bentsen, G. & Schleier-Smith, M. Approaching the Heisenberg limit without single-particle detection. *Phys. Rev. Lett.* **116**, 053601 (2016).

47. Kaubruegger, R., Vasilyev, D. V., Schulte, M., Hammerer, K. & Zoller, P. Quantum variational optimization of Ramsey interferometry and atomic clocks. *Phys. Rev. X* **11**, 041045 (2021).

48. Colombo, S. et al. Time-reversal-based quantum metrology with many-body entangled states. *Nat. Phys.* **18**, 925–930 (2022).

49. Pezzè, L. & Smerzi, A. Quantum phase estimation algorithm with Gaussian spin states. *PRX Quantum* **2**, 040301 (2021).

50. Zhang, X. et al. Spectroscopic observation of SU(N)-symmetric interactions in Sr orbital magnetism. *Science* **345**, 1467–1473 (2014).

51. Bromley, S. L. et al. Dynamics of interacting fermions under spin–orbit coupling in an optical lattice clock. *Nat. Phys.* **14**, 399–404 (2018).

52. Muniz, J. A. et al. Exploring dynamical phase transitions with cold atoms in an optical cavity. *Nature* **580**, 602–607 (2020).

53. Vaidya, V. D. et al. Tunable-range, photon-mediated atomic interactions in multimode cavity qed. *Phys. Rev. X* **8**, 011002 (2018).

54. Davis, E. J. et al. Protecting spin coherence in a tunable Heisenberg model. *Phys. Rev. Lett.* **125**, 060402 (2020).

55. Dogra, N. et al. Dissipation-induced structural instability and chiral dynamics in a quantum gas. *Science* **366**, 1496–1499 (2019).

Methods

Atomic state preparation

[87]Sr atoms were laser-cooled and trapped in a two-stage magneto-optical trap located ~40 mm below the cavity, where the atoms were subsequently loaded into the vertical optical lattice formed by two counter-propagating 813 nm beams. The relative phase of the optical lattice was detected by interfering the two beams in a Mach–Zender interferometer and we stabilized the optical lattice phase by feeding back to an acousto-optic modulator (AOM) on the bottom-up lattice beam with ~1 kHz bandwidth.

Once cooled and trapped in the lattice, the atoms were optically pumped into the $|m_F = -9/2\rangle$ hyperfine ground state. To transport the atoms vertically into the cavity, the frequency of the bottom-up lattice beam was linearly ramped and detuned by δ_l, resulting in a moving lattice with a velocity of $\upsilon(t) = \frac{\delta_l(t)\lambda_l}{4\pi}$ (ref. [56]). To select the atoms with the lowest temperature, we applied a ramp of the optical lattice trap depth down to $7E_r$ and then back up to our operation depth of $20E_r$, which allowed the hot atoms to escape the trap. E_r is the recoil energy of an optical lattice photon. We applied a bias magnetic field of 2 G along the direction of the cavity (Fig. 1a). To ensure high spin-state purity of our atoms, a clock π-pulse of 40 ms was applied on the $|^1S_0, m_F = -9/2\rangle \rightarrow |^3P_0, m_F = -9/2\rangle$ transition and the atoms remaining in the ground state were removed by applying a light pulse tuned to the $|^1S_0\rangle \rightarrow |^1P_1\rangle$ 461 nm transition. After these preparation steps, we had an ensemble of atoms with the radial temperature of 290(10) nK and vertical cloud size of 130 μm. Although here we operated on a single transition, in the future we will be able to probe both stretched states ($|^1S_0, m_F = \pm 9/2\rangle \rightarrow |^3P_0, m_F = \pm 9/2\rangle$), to reject magnetic field noise. This will require different state preparation and further modifications to the cavity probing set-up to adjust the cavity frequency for each shot of the experiment to probe each spin state.

Optical local oscillator

The clock local oscillator was a 698 nm fibre laser prestabilized by a 40 cm ultralow expansion glass cavity. This 698 nm laser was phase locked to a frequency comb that was stabilized by a 21 cm crystalline silicon cavity operating at 124 K (refs. [15,38]). A portion of the fully stabilized 698 nm light seeded an injection locked laser, which was then delivered to the experiment by means of a fibre-noise cancelled optical fibre. The first order of an AOM was used to probe the atomic resonance and the zeroth order of the AOM served as the phase reference for the fibre-noise cancellation. Differential noise between the zeroth and first order was minimized using beam tubes and multiple layers of isolation from acoustic noise.

Optical cavity and QND probe

The optical cavity with cavity length of $L = 6.9720(2)$ cm supported a TEM00 mode with a $1/e^2$ beam waist of $w_0 = 71$ μm and had a power-decay rate of $\kappa = 2\pi \times 158(7)$ kHz. The radius of curvature for each mirror was 5 cm. The cavity was one-sided such that the transmission coupling rate of the input mirror κ_1 was much greater than that of the back mirror, κ_2. The cavity was isolated from vibrations by suspending the spacer in a double-pendulum configuration, using Viton as the lossy springs. The vibration isolation resulted in a roll-off in vibration noise coupling above ~30 Hz.

We stabilized the cavity length to a prestabilized 813 nm laser by means of Pound–Drever–Hall locking, feeding back to the cavity piezo transducer (PZT) with a bandwidth of ~1 kHz. The intracavity 813 nm light was set to a low intensity such that the resulting trap depth was much less than $1E_r$. A conservative estimate of the clock frequency shift due to this beam was of the order of 10^{-18}. The 813 nm extended cavity diode laser (ECDL) was prestabilized by means of a phase lock to the same frequency comb that transferred the clock local oscillator phase. For the QND probe light, an ECDL at 689 nm was stabilized to a Hz-level optical cavity and at low frequency, stabilized to the frequency comb. A phase-modulated sideband at 137.59 MHz was then generated by a fibre electro-optic modulator (EOM) to probe the cavity. We set the probe photon number by changing the modulation depth of the EOM drive. The technical noise floor of the entire locking chain was evaluated by probing the empty cavity at a probe photon number of ~10^6 per measurement window. The standard deviation of two repeated bare cavity frequency measurements yielded 200 Hz, which was approximately 20 dB below the QPN limit. Atoms trapped in the vertical 1D optical lattice had a longitudinal trap frequency of 25 kHz and a radial trap frequency 34 Hz. The duration of each QND measurement was chosen to be 40 ms to average the single-particle motional effects of atoms.

Balanced homodyne detection

We measured the phase shift of the probe laser in the reflection port of the cavity using homodyne detection against a reference local oscillator (LO) (Fig. 1a). A similar experimental set-up for homodyne detection was implemented in ref. [25]. The homodyne fringe was detected using a home-built balanced photodetector, where we took the difference between the two output ports of the homodyne beamsplitter. The combination of active stabilization of the LO intensity and the common-mode rejection of the LO intensity noise allowed the homodyne detection to be photon shot noise limited. The technical dark noise of the photodetector was ~31 dB below the LO photon shot noise. We stabilized the phase of the carrier with respect to the LO by detecting the carrier-LO beat note and phase locking it to a reference radio frequency synthesizer. By stabilizing this phase, we removed any path length fluctuations that arose in the differential path between the probe beam and the LO. The power in the carrier was approximately 150 nW, so the photon shot noise of this phase lock was negligible compared with the probe sideband.

Vibrations of the optical breadboard couple to the homodyne output voltage by means of differential pointing instabilities of the LO beam through the interferometer. An accelerometer placed on the table near the homodyne interferometer showed strong correlations with the homodyne output voltage at ~20 Hz and ~30 Hz, coming from air conditioning motor vibrations. In our data recording, the table vibrations were synchronously sampled with our homodyne measurements. We subtracted the vibrations multiplied by a scale factor in the analysis step, but it could have been implemented in real-time with relative ease. Once the optical alignment was finalized, the optimal scale factor of the vibrations to homodyne voltage remained constant.

Effective atom–cavity coupling

To experimentally determine g, we measured the magnitude of the differential cavity frequency shift noise, denoted by $\Delta(\omega_\downarrow - \omega_\uparrow)$, versus the sum shift $\omega_{sum} = \omega_\downarrow + \omega_\uparrow$. We required an expression for this noise in terms of the sum shift with g as a fitting parameter. The frequency shifts of the cavity mode for the $|\downarrow\rangle$ and $|\uparrow\rangle$ states were

$$\omega_{\downarrow,\uparrow} = \frac{-\delta_c - \sqrt{\delta_c^2 + \Omega_{\downarrow,\uparrow}^2}}{2}, \qquad (2)$$

where the vacuum Rabi splittings for each spin state were $\Omega_\downarrow = 2g\sqrt{N_\downarrow}$ and $\Omega_\uparrow = 2g\sqrt{N_\uparrow}$. The QPN fluctuation of the frequency shift was obtained using the derivative, $\Delta\omega_\downarrow = |\frac{d\omega_\downarrow}{dN_\downarrow}|\Delta N_\downarrow$. Solving the eigenvalue expression equation (2) for $N_\downarrow$ with a negative δ_c gives

$$N_\downarrow = \frac{\omega_\downarrow(\delta_c + \omega_\downarrow)}{g^2}. \qquad (3)$$

Note that both δ_c and the frequency shift $\omega_\downarrow$ are negative quantities. For a CSS of N total atoms prepared by a π/2 pulse on the equator of

the Bloch sphere with state population $N_\downarrow = N_\uparrow = N/2$, one can express N in terms of the sum of measured frequency shifts $\omega_{\text{sum}} = \omega_\downarrow + \omega_\uparrow$ as

$$N = \omega_{\text{sum}} \frac{\delta_c}{g^2} \left(1 + \frac{1}{2} \frac{\omega_{\text{sum}}}{\delta_c}\right). \tag{4}$$

QPN for the two spin states was $\Delta N_\downarrow = \Delta N_\uparrow = \sqrt{N}/2$. We calculated the projection noise fluctuations of the frequency shift using the derivative of the eigenvalue expression. Projection noise fluctuations of $N_\downarrow$ and $N_\uparrow$ are perfectly anticorrelated and therefore $\Delta(\omega_\uparrow - \omega_\downarrow)$ is twice the fluctuations of $\omega_\downarrow$,

$$\Delta(\omega_\uparrow - \omega_\downarrow) = 2\Delta\omega_\downarrow = \frac{g^2\sqrt{N}}{\sqrt{\delta_c^2 + \Omega_\downarrow^2}}. \tag{5}$$

Using equations (4) and (5), the expression for characterizing g based on the measurement on QPN fluctuations of the initial CSS was

$$\Delta(\omega_\uparrow - \omega_\downarrow) = g\sqrt{\frac{\omega_{\text{sum}}^2/2 + \delta_c \omega_{\text{sum}}}{(\omega_{\text{sum}} + \delta_c)^2}} \tag{6}$$

To account for technical measurement noise in the absence of atoms ($\omega_{\text{sum}} = 0$), we fitted equation (6) with an offset term added in quadrature. At high atom numbers, rotation noise became noticeable in the QPN measurement. We experimentally determined the rotation noise by performing a $\pi/2$ pulse $- N_\downarrow - 2\pi$ pulse $- N_\downarrow$. We then scaled this noise by the ratio $(2/1.5)$, which is the ratio of the clock pulse area for the rotation noise measurement to the QPN measurement. The rotation noise was then subtracted in quadrature from the QPN measurement. Our final result was a value of $g = 2\pi \times 5.1(2)$ kHz, with the bare cavity noise offset of $2\pi \times 0.76(5)$ kHz. With the value of g in hand, we converted our frequency shift noise to J_z noise as plotted in Fig. 2a.

The effective atom–cavity coupling g was independently estimated as a consistency check on our experimentally determined value from Fig. 2a. We followed the convention from[41], where the effective g is

$$g^2 = \frac{\langle g_i^4 \rangle}{\langle g_i^2 \rangle}, \tag{7}$$

where g_i is the atom–cavity coupling for the ith atom. The effective atom number was

$$N = N_{\text{tot}} \frac{\langle g_i^2 \rangle^2}{\langle g_i^4 \rangle} \tag{8}$$

where N_{tot} is the total atom number. In this work, when we refer to g and N, we refer to the effective quantities. Our coordinate system is defined such that X is the direction along the cavity axis, Y is the other horizontal axis orthogonal to X and Z is the vertical direction along gravity. The atomic density distribution in Z was modelled as a Gaussian, $\rho_Z(Z) = \frac{N}{\sqrt{2\pi}\sigma_Z} e^{-Z^2/(2\sigma_Z^2)}$, with standard deviation σ_Z. The probability distribution along Y was $P_Y(Y) = \frac{1}{\sqrt{2\pi}\sigma_Y} e^{-Y^2/(2\sigma_Y^2)}$, which is a Gaussian with a standard deviation σ_Y set by the thermal cloud radius. We calculated σ_Y from the radial temperature of $T_r = 290(10)$ nK from a radial Doppler scan of the clock transition and the radial trap frequency of 34(3) Hz. If we allowed the atoms to sufficiently time-average the standing wave along X, then

$$g_i^2(Y, Z) = \frac{g_0^2}{2} e^{-2(Y^2 + Z^2)/w_0^2} \tag{9}$$

with peak coupling $g_0 = d_0 \sqrt{\frac{\omega_p}{2\epsilon_0 \hbar V}} = 2\pi \times 8.6$ kHz. Here, d_0 is the dipole matrix element and ω_p is the angular frequency of the $|\downarrow\rangle \to |e\rangle$ transition and $V = \frac{1}{4}\pi\omega_0 L$ is the effective cavity mode volume. The ensemble averages were evaluated as

$$\langle g_i^2 \rangle = \frac{1}{N} \int g_i^2(Y, Z) \rho_Z(Z) P_Y(Y) \, dY dZ \tag{10}$$

and

$$\langle g_i^4 \rangle = \frac{1}{N} \int g_i^4(Y, Z) \rho_Z(Z) P_Y(Y) \, dY dZ, \tag{11}$$

and when combined using equation (7) give the estimated value of $g = 2\pi \times 4.8(2)$ kHz.

Quantum efficiency

The overall quantum efficiency of the measurement plays a key role in QND-based spin squeezing. The amount of attainable spin squeezing is linearly proportional to the quantum efficiency[57]. Furthermore, $Q < 1$ leads to excess noise in the antisqueezed quadrature. We first estimated the overall quantum efficiency by considering the different contributions, including the cavity quantum efficiency $\kappa_1/\kappa = 0.68$, mode overlap of the cavity leakage light and the homodyne LO beam of 0.75, quantum efficiency of the photodiode of 0.88 and finite path efficiency of 0.62 and other negligible sources. Multiplying these together gives a quantum efficiency of $Q = 0.28$. We used this value when estimating the expected R (cyan line in Fig. 3c), which shows reasonable agreement. The measured noise level at the antisqueezed quadrature was 9 dB above what was expected from the estimated quantum efficiency (Fig. 2d). This indicates an additional noise source contributing to the antisqueezing, but it does not preclude observing the benefit of spin squeezing.

Independence of the atomic subensembles

To assess the independence of the subensembles, we varied the vertical separation between the ensembles and evaluated the Pearson correlation coefficient between the measured J_z for each ensemble. We expected that for no separation (probing the same ensemble) there would be high correlation between the measured QPN, and that as we increased the separation distance the correlation coefficient would decrease. We first measured $J_{z,A}$ for ensemble A, applied a vertical displacement of the cloud by means of the movable optical lattice to put ensemble B in the cavity and subsequently measured $J_{z,B}$. The measured correlation coefficient between $J_{z,A}$ and $J_{z,B}$ is shown versus the separation distance between the ensembles in units of the mode waist w_0 (Extended Data Fig. 1). The blue line is a numerical Monte Carlo simulation of the correlation coefficient for two ensembles with varying mean separation. We also calculated the change of the combined QPN versus the separation distance using both analytical and numerical methods (Extended Data Fig. 1b). For the differential clock comparisons of Fig. 4, a spatial separation of 150 µm (dashed grey line) was chosen to guarantee independence of the ensembles.

Differential clock comparison

The timing sequence for the differential clock comparison includes clock rotations, transports and QND measurements (Extended Data Fig. 2a). Clock pulses are shown as black pulses, with the pulse area and axis of rotation shown. Transport steps are indicated by the green and purple pulses and the transport waveform for the optical lattice detuning are linear ramps of the frequency over 5 ms. All clock pulses were applied with the lattice at the same vertical location, so we did not have to take into account the varying clock laser phase. After the premeasurements, the $\frac{\pi}{2}|_x$ clock pulse rotated the spin-squeezed axis to the

phase-sensitive axis. After a total evolution time of $T = 14$ ms, the final $\pi/2$ pulse rotated back to the J_z-basis for readout. This final $\pi/2|_\phi$ pulse was rotated about an axis ϕ, which, for our relatively short Ramsey dark time, was approximately along the x axis of the Bloch sphere. The phase ϕ was chosen to result in a final Bloch vector near the equator for maximal phase sensitivity. The final measurements were taken at a higher probe photon number than the premeasurements. The CSS–CSS comparison used the same pulse sequence, but the premeasurements had no probe light applied. For both the CSS–CSS and SSS–SSS comparisons, we observed a fractional frequency difference at the 10^{-15} level, which is likely to have arisen from leakage of the LO light used for cQED homodyne detection, which will be mitigated in future experiments. We set the separation between the two ensembles such that the two atom numbers were $N_A \approx 8{,}800$ and $N_B \approx 8{,}500$.

The pre and final measurements for each ensemble constitute cavity frequency shifts for each spin state. Making use of the eigenvalue expression for the atom–cavity system (see equation (3)), we converted these frequency differences to atom number differences, labelled $dN = N_\downarrow - N_\uparrow$. To convert the measured atom number differences directly to phase, we scanned out the Ramsey fringe (Extended Data Fig. 2b). The fitted amplitude of this fringe α was used to convert the measured atom number difference for each ensemble to differential phase (in the small angle limit),

$$\phi_A - \phi_B = \frac{(dN_{A,f} - \beta_A dN_{A,p}) - \beta_D(dN_{B,f} - \beta_B dN_{B,p})}{\alpha}, \quad (12)$$

where we have introduced optimal estimators β_A, β_B for the premeasurements and β_D for the differential noise of ensembles A and B. The three parameters were simultaneously optimized to give the smallest $\Delta(\phi_A - \phi_B)$. By varying the length of the dataset from half the length to the full length, we took the mean and standard deviation of each optimal estimator. The values were $\beta_A = 0.49(1)$, $\beta_B = 0.48(1)$ and $\beta_D = 0.907(5)$ (Extended Data Fig. 2c,d). The slight deviation of β_D from unity indicates some small asymmetric noise between the ensembles. This could arise from inhomogeneous ac Stark shifts, unequal squeezing of the ensembles, or differential thermal motion affecting clock rotations. This β_D is accounted for in the estimated effective SQL for the clock comparison,

$$\Delta(\phi_A - \phi_B)_{eff-SQL} = \sqrt{\frac{1}{C_i N_A} + \beta_D^2 \frac{1}{C_i N_B}}. \quad (13)$$

The phase resolution is converted to the fractional frequency Allan deviation by multiplying by the slope of the Ramsey fringe

$$\sigma_{y,eff-SQL}(\tau) = \frac{\sqrt{T_{cycle}/\tau}}{2\pi\nu_0 T} \sqrt{\frac{1}{C_i N_A} + \beta_D^2 \frac{1}{C_i N_B}}, \quad (14)$$

where $T_{cycle} = 5.5$ s is the cycle time of the experiment. This cycle time is limited by the blue magneto optical trap (MOT) loading time needed to maximize atom number— future improvements in atom loading efficiency will thus improve the fractional frequency stability. The expression for the QPN-limited frequency stability is the same apart from a factor of $1/\sqrt{C_i}$,

$$\sigma_{y,QPN}(\tau) = \frac{\sqrt{T_{cycle}/\tau}}{2\pi\nu_0 T C_i} \sqrt{\frac{1}{N_A} + \beta_D^2 \frac{1}{N_B}}. \quad (15)$$

We note that the decibel gain value for the differential clock comparisons were calculated for QPN (effective SQL) using $20\log_{10}(\sigma_{y,measured}/\sigma_{y,QPN(eff-SQL)})$, respectively.

Squeezing metrics and metrological enhancement
To quantify the degree of metrological enhancement, we took into account the non-unity initial contrast $C_i < 1$ in equation (1). This metric has been used in previous works to demonstrate entanglement in a spin-squeezed ensemble[23,25] under the assumption that cavity probing decreases the coherence of the ensemble (that is, it cannot increase the spin correlations in the transverse plane)[42]. The technical limitation of the initial contrast is taken into account in the metrological enhancement due to squeezing by comparing the same experimental sequence with and without the QND measurements, as depicted in Fig. 3a. The Wineland parameter, $\bar{\xi} = \xi/C_i = \left(\frac{\Delta(J_{z,f} - \beta J_{z,p})}{\Delta J_{z,QPN}}\right)^2 \frac{1}{C_f^2}$[18], did not consider the experimental fact of a non-unity initial contrast. For reference, the single-ensemble measurement of Fig. 3 gives a value for this initial Wineland parameter of $\bar{\xi} = -0.2(7)$ dB. In our system, this initial contrast was limited by the inhomogeneous optical rotations by means of coupling to atomic motion. Properly accounting for the $C_i = 0.71(1)$ limited by these optical rotations, we achieved a metrological enhancement of $\xi = -1.7(7)$ dB, which demonstrates the generation of entanglement in a single ensemble (subject to these eminently reasonable physical assumptions).

For the two-clock ensemble comparisons, we compared the full clock interrogation sequence with all rotations needed for squeezing, in one case omitting QND probing for the CSS–CSS comparison and in the other performing the QND measurements to compare two squeezed ensembles. The QPN-limited stability of equation (15) is the fractional frequency stability when the differential measurements are limited by the QPN for the effective ensemble size of $C_i N$ atoms. We note that the achievement of QPN-limited CSS–CSS performance is a feat in itself: this requires both QPN-limited readout sensitivity (demonstrated in Fig. 2a) and pristine control of the local oscillator phase, as the Ramsey interferometer introduces sensitivity to differential phase noise. Interferometer performance beyond equation (15) can only be obtained by non-classical correlations with the introduction of spin squeezing, for a given initial contrast C_i. This QPN-stability metric thus provides a benchmark for the practical improvement in stability due to the QND measurements.

Data availability
The experimental data presented in this article are available from the corresponding author upon reasonable request. Source data are provided with this paper.

Code availability
The code used for analysis and simulation in this work is available from the corresponding author upon reasonable request.

References
56. Sauer, J., Fortier, K., Chang, M., Hamley, C. & Chapman, M. Cavity QED with optically transported atoms. *Phys. Rev. A* **69**, 051804 (2004).
57. Chen, Z., Bohnet, J. G., Weiner, J. M., Cox, K. C. & Thompson, J. K. Cavity-aided nondemolition measurements for atom counting and spin squeezing. *Phys. Rev. A* **89**, 043837 (2014).

Author contributions

All authors contributed to the design and operation of the experiment and data analysis and writing of the manuscript.

Competing interests

The authors declare no competing interests.

Additional information

Extended data is available for this paper at https://doi.org/10.1038/s41567-023-02310-1.

Supplementary information The online version contains supplementary material available at https://doi.org/10.1038/s41567-023-02310-1.

Correspondence and requests for materials should be addressed to John M. Robinson or Jun Ye.

Peer review information *Nature Physics* thanks Luca Pezze and the other, anonymous, reviewer(s) for their contribution to the peer review of this work.

Reprints and permissions information is available at www.nature.com/reprints.
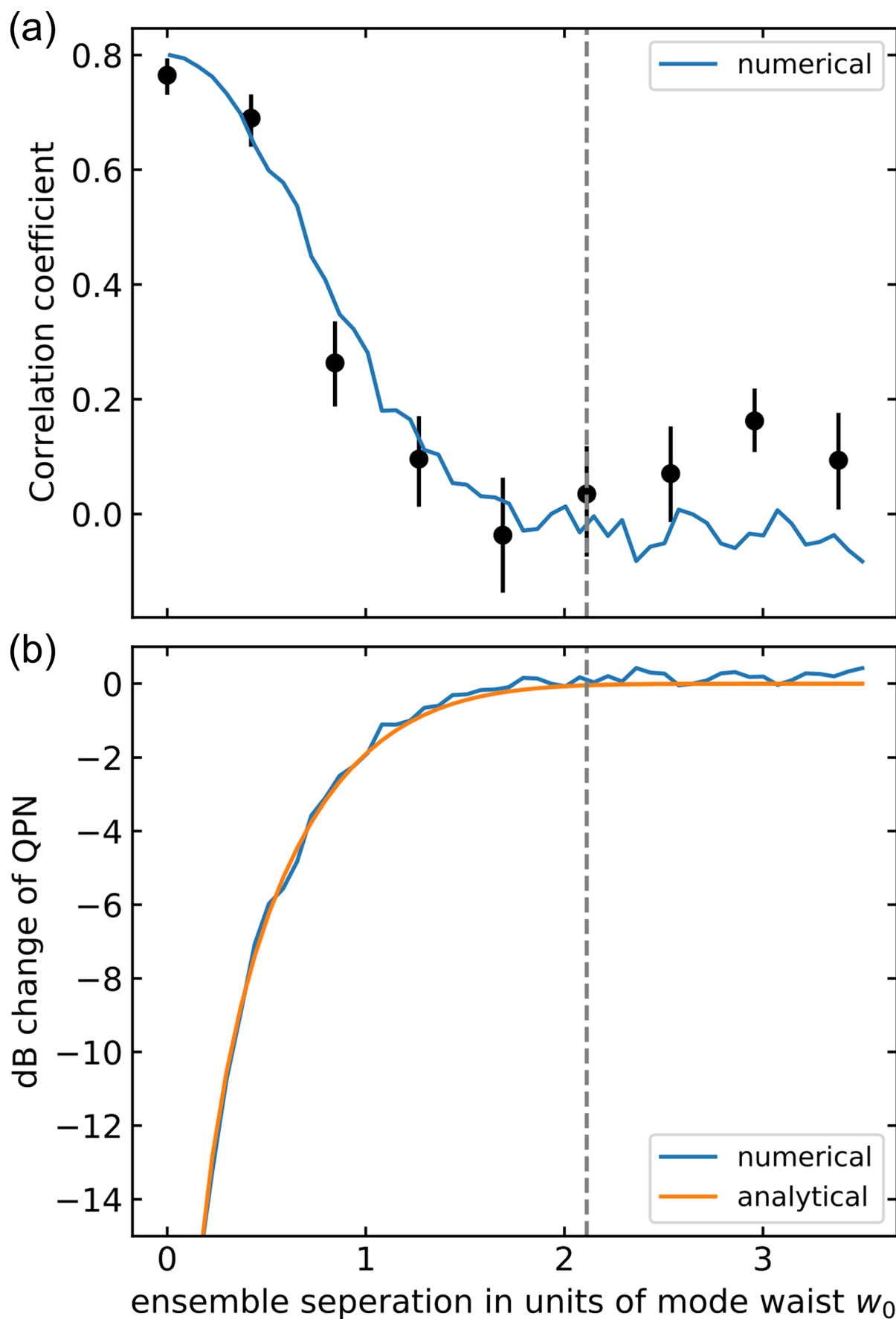
Extended Data Fig. 1 | Independence of atomic ensembles. a, Measured correlation coefficient between $J_{z,A}$ and $J_{z,B}$ versus the separation between the ensembles. (black circles). The blue line is a Monte Carlo simulation. **b,** Corresponding change of the QPN due to the finite overlap of the ensembles, with numerical Monte Carlo simulation (blue) and analytical calculation (orange). At our operating ensemble separation, the change to QPN is 0.04 dB.
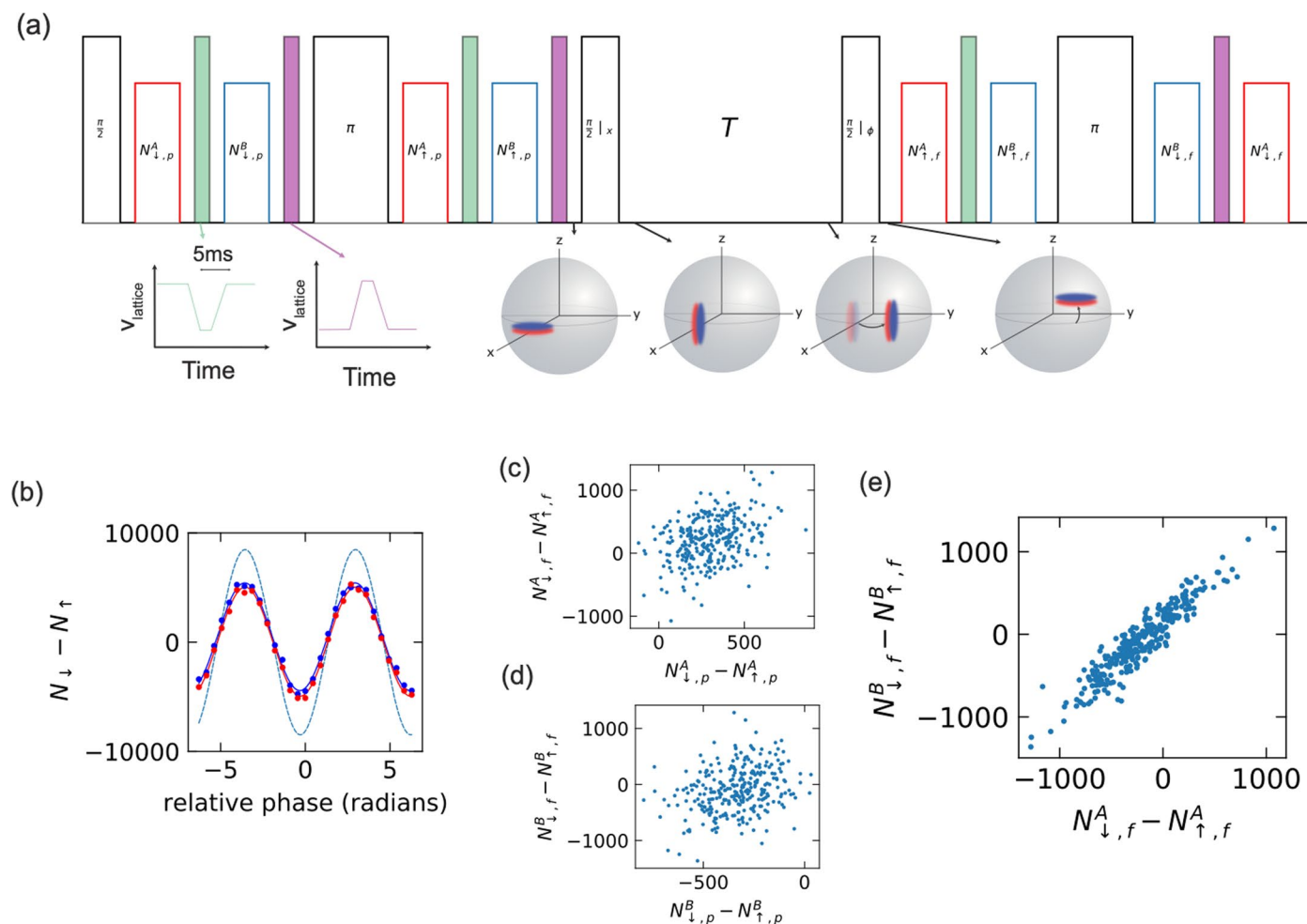
Extended Data Fig. 2 | Pulse sequence for SSS - SSS comparison. a, Clock pulses are the black pulses, measurements of ensemble A are the red pulses, and the transports are shown as the green and purple pulses. The Bloch spheres depict the spin state distribution at various points during the sequence. We note that the phase evolution is exaggerated for clarity. **b**, Ramsey fringe measured by varying the phase of the final π/2 pulse. **c**, Pre and final measurements of ensemble A. **d**, Pre and final measurements of ensemble B. **e**, The final measurements of ensemble A and B show strong correlations, allowing for the subtraction of the common-mode laser phase noise. The data in panels (b-e) correspond to the raw data corresponding to the SSS-SSS comparison shown in Fig. 4b.